

An excursion set model of the cosmic web: The abundance of sheets, filaments and halos

Jiajian Shen

*Department of Astronomy and Astrophysics, The Pennsylvania State University,
University Park, PA 16802*

Tom Abel

*Kavli Institute for Particle Astrophysics and Cosmology, Stanford Linear Accelerator
Center, 2575 Sand Hill Road, MS 29, Menlo Park, CA 94025*

H.J. Mo

Department of Astronomy, University of Massachusetts, Amherst MA 01003

and

Ravi K. Sheth

*Department of Physics and Astronomy, University of Pennsylvania, 209 South 33rd Street,
Philadelphia, PA 19104*

ABSTRACT

We discuss an analytic approach for modeling structure formation in sheets, filaments and knots. This is accomplished by combining models of triaxial collapse with the excursion set approach: sheets are defined as objects which have collapsed along only one axis, filaments have collapsed along two axes, and halos are objects in which triaxial collapse is complete. In the simplest version of this approach, which we develop here, large scale structure shows a clear hierarchy of morphologies: the mass in large-scale sheets is partitioned up among lower mass filaments, which themselves are made-up of still lower mass halos. Our approach provides analytic estimates of the mass fraction in sheets, filaments and halos, and its evolution, for any background cosmological model and any initial fluctuation spectrum. In the currently popular Λ CDM model, our analysis suggests that more than 99% of the cosmic mass is in sheets, and 72% in filaments, with mass larger than $10^{10} M_\odot$ at the present time. For halos, this number is only 46%. Our approach also provides analytic estimates of how halo abundances at any given time correlate with the morphology of the surrounding large-scale structure, and how halo evolution correlates with the morphology of large scale structure.

Subject headings: structure formation: ellipsoidal collapse – mass functions: sheets, filaments, halos

1. Introduction

Recent observations and high resolution numerical simulations of structure formation show that, on large scales, the Universe is best thought of as a Cosmic Web (Bond, Kofman & Pogosyan 1996): large scale sheets are traversed by filaments, which themselves intersect at knots (Bhavsar & Ling 1988; Bharadwaj et al. 2000; Bhavsar et al. 2003; Sheth et al. 2003; Bharadwaj & Biswajit 2004; Shandarin et al. 2004; Biswajit & Bharadwaj 2005; Colberg et al. 2005), and there are vast relatively empty voids in between (Gregory & Thompson 1982; Kirshner et al. 1983; Müller et al. 2003; Vogeley et al. 2004). The knots where filaments intersect are the locations of rich galaxy clusters, and these are often identified with the massive virialized dark matter halos found in simulations. Halos are the best-studied features of the cosmic web; they tend to be about two hundred times denser than the background universe, so they account for a small fraction of the volume of the Universe. Simple analytical models have been very successful in understanding the properties of dark halos (Gunn & Gott 1972; Press & Schechter 1974; Bond et al. 1991). However, with the exception of Zeldovich (1970) and Gurbatov, Saichev & Shandarin (1989), a framework for describing the properties and dynamics of filamentary and sheet-like structures in the cosmic web is still lacking. The main goal of this paper is to provide such a framework: our goal is to discuss the cosmic web using language which extends naturally that currently used for discussing dark halos. This complements recent work showing how the same framework can be used to discuss cosmic voids (Sheth & van de Weygaert 2004).

In current descriptions of large scale structure, the abundance by mass of dark matter halos and the evolution of this abundance, i.e., the cosmological mass function $n(M, z)$, plays a fundamental role. Models of this mass function suggest that it encodes information about both gravitational dynamics and the statistics of the initial fluctuation field (Press & Schechter 1974; Bond et al. 1991). Models of $n(M, z)$ which assume that dark halos form from a spherical collapse are in reasonable but not perfect agreement with results from numerical simulations of hierarchical gravitational clustering (Sheth & Tormen 1999). In reality, halos are triaxial (Jing & Suto 2002), so they cannot have formed from a spherical collapse. The initial shear field and tidal effects almost certainly play some role in determining the evolution of an object, and models of the associated non-spherical collapse have been developed (Zeldovich 1970; Icke 1973; White & Silk 1979; Peebles 1980; Bond & Myers 1996). Such non-spherical collapse models can be incorporated into models of the halo mass function in various ways (Eisenstein & Loeb 1995; Monaco 1995; Lee & Shandarin 1998; Chiueh & Lee

2001). In particular, Sheth et al. (2001) argued that much of the discrepancy between model predictions and simulations is removed if one replaces the assumption of a spherical collapse with one where halos form from a triaxial collapse.

In this paper, we exploit a crucial difference between spherical and ellipsoidal collapse models of halo formation. Namely, if we think of a halo as being triaxial, then the formation of an object corresponds to the time when gravity has caused all three axes to turn around from the universal expansion and collapse (Sheth et al. 2001). If the object is spherical, this collapse occurred at the *same* time for all three axes. In contrast, a triaxial object has three critical times, corresponding to the collapse along each of the three axes—the shortest axis collapses first, the intermediate axis later and the longest axis last.

If we identify ‘halos’ with objects which have collapsed along all three axes, then it is natural to identify filaments with objects which have collapsed along only two axes, and sheets with objects which have only collapsed along one axis. Given this identification, the remainder of this paper describes how to construct a model which naturally encapsulates the idea that halos form within filaments which themselves populate sheets. In particular, we provide a framework for discussing the mass functions of sheets and filaments, and how these evolve, as well as the conditional mass functions of halos within filaments and sheets, and their evolution.

Section 2 presents our model. It begins with a discussion of our triaxial collapse model (Section 2.1). Appendix A compares this model with others in the literature. It then translates this model into a form which is most convenient for use in the ‘excursion set’ approach (Sections 2.2—2.4). The excursion set approach is commonly used to estimate the mass function of halos (Bond et al. 1991; Sheth et al. 2001). Our collapse model, when combined with the excursion set approach, has a rich structure. We illustrate this by using it to generate analytic approximations to the mass functions of sheets and filaments (Section 2.5), and to the conditional distributions of filaments in sheets, and halos in filaments (Section 2.6). Comments on how mass accretion may depend on environment (Section 2.7), and on the characteristic densities of sheets, filaments and halos, which may aid identification of such objects in the cosmic web (Section 2.8) conclude this section. Section 3 summarizes our findings.

2. A model for sheets, filaments and halos

2.1. Ellipsoidal collapse

The gravitational collapse of homogeneous ellipsoids was studied by Icke (1973), White & Silk (1979), and Peebles (1980). Although the exact evolution must be solved-for numerically, White & Silk (1979) provide an elegant analytic approximation for the evolution which is remarkably accurate. Unfortunately, these early analysis did not reduce, as they should, to the Zeldovich approximation in the linear regime. Bond & Myers (1996) noted that this was because they did not include the effects of the external tide self-consistently; once these effects are included, the collapse model is indeed self-consistent. Appendix A provides details, and also shows how the analysis of White & Silk (1979) can be extended to this self-consistent case. In this model, the initial collapse is expected to be dominated by the local strain tensor, which includes both internal and external tidal forces. For any given cosmology, the evolution of a patch in this model is determined by three quantities: its initial overdensity, δ , and two shape parameters, e and p . It is this model which we will use in what follows.

2.2. Mass functions and random walks: Three barriers for three axes

In the ‘excursion set’ approach (Bond et al. 1991), an approximation for the mass fraction in bound virialized halos of mass m is obtained by mapping the problem to one which involves the first crossing distribution of a suitably chosen barrier by Brownian motion random walks. The choice of barrier is set by the collapse model and by the epoch for which one wishes to estimate the mass function, and the mapping between random walk variables and halo masses is set by the shape of the power spectrum of the initial fluctuation field.

In particular, if $f(\nu)$ denotes the fraction of walks which first cross a barrier at scale ν , where ν is the random walk variable, then the mass fraction in objects of mass m is

$$\nu f(\nu) \equiv m^2 \frac{n(m, z)}{\rho_{m_0}} \frac{d \ln m}{d \ln \sigma^2} \quad (1)$$

(Bond et al. 1991). Here $\sigma^2(m)$ is the variance in the initial density fluctuation field, smoothed on scale $R = (3m/4\pi\rho_{m_0})^{1/3}$, and extrapolated using linear theory to the present time.

If the collapse is spherical, then the barrier is particularly simple: it has constant height, with higher barriers required to model the halo population at higher redshift. In particular, this height is very simply related to the initial overdensity required for spherical collapse by redshift z . This value, which is usually denoted $\delta_{sc}(z)$, will play a special role in what follows.

In the ellipsoidal collapse model, the barrier height associated with halo formation by redshift z depends on three numbers: the initial overdensity, and the shape parameters e and p . In principle, then, the problem of estimating the mass function is one of crossing a barrier in a higher dimensional space (Sheth et al. 2001; Chiueh & Lee 2001; Sheth & Tormen 2002). Sheth et al. (2001) suggested that the computational complexity could be reduced significantly if one used suitably chosen representative values of e and p . Once these have been set (for reasons given in Appendix A, they suggested $p = 0$ and $e = [\sigma(m)/\delta]/\sqrt{5}$), the excursion set approach corresponds to finding the first crossing distribution by a *one-dimensional* random walk in δ of a barrier whose height is *mass-dependent*. In this respect, the estimation of the mass function associated with ellipsoidal collapse proceeds exactly as for spherical collapse—the only complication is that the barrier height is no longer constant.

Our model for the mass function in filaments and sheets is entirely analogous. In principle, filaments at z can form from some combination of δ , e and p ; the precise combination depends on the details of the collapse model. In our preferred model, the same one used by Sheth et al. (2001), this requires that collapse occurs along the intermediate length axis at z , but along the longest axis at a later time. Thus, estimation of the mass fraction in filaments requires solution of a high-dimensional random walk, and, as for collapse along all three axes, we approximate by setting e and p equal to representative values, and considering a one-dimensional walk in the remaining variable δ . In this case, the barrier height associated with filament formation is that associated with collapse along two, rather than three axes. And a similar argument means that the mass function in sheets can be approximated by studying the first crossing distribution of the one-dimensional barrier associated with collapse along just one axis.

Figure 1 illustrates the basic idea. The jagged line shows a random walk, and the three dotted lines show the barriers associated with collapse along one (bottom), two (middle) and three (top) barriers. In our model, the fraction of walks which first cross the lowest barrier on scale $\sigma(m)$ equals the mass fraction in sheets of mass m , the fraction which first cross the second barrier at $\sigma(m)$ equals the mass fraction in filaments of mass m , and the fraction which first cross the highest barrier at $\sigma(m)$ equals the mass fraction in triaxial halos of mass m . We will provide estimates of these quantities shortly.

However, Figure 1 shows that this model can also be used to provide significantly more information. For instance, notice that all walks first-cross the barrier associated with sheets at a higher mass scale than when they first-cross the barriers associated with filaments or halos. Thus, in addition to providing a way to estimate the mass functions of sheets, filaments and halos, our approach also provides a framework for discussing the mass fraction in halos of mass m_h that are embedded in filaments of mass $m_f < m_s$ which are themselves surrounded by sheets of mass $m_s > m_f$. Figure 1 shows that this is simply related to the

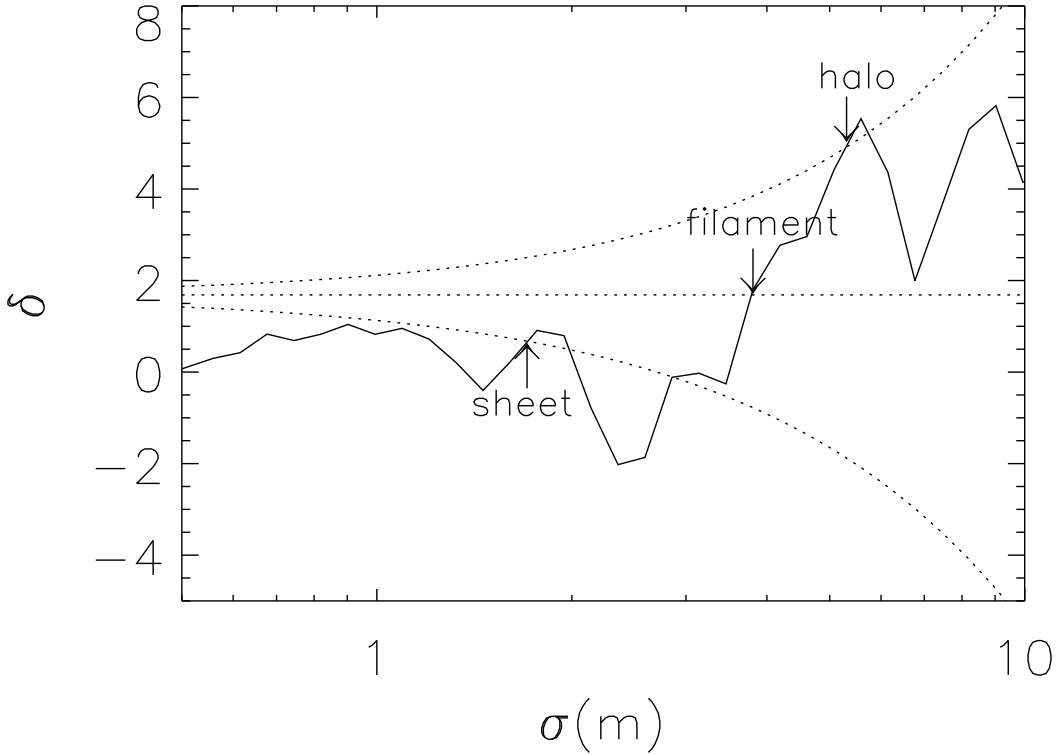


Fig. 1.— An example of a random walk (solid line) crossing the barriers (dotted lines) associated with sheets, filaments and halos (bottom to top). The fraction of walks which first cross the lowest barrier at $\sigma(m_s)$, then first cross the second barrier at $\sigma(m_f)$ and finally cross the highest barrier at $\sigma(m_h)$ represents the mass fraction in halos of mass m_h which are embedded in filaments of mass $m_f > m_h$, which themselves populate sheets of mass $m_s > m_f$ (recall that σ is a decreasing function of m). The precise barrier shapes depend on the collapse model; the dotted curves show the barriers in equation (2).

fraction of walks which are conditioned to pass through certain points before first crossing m_h . Thus, our approach allows one to estimate how halo abundances correlate with the *morphology* and density of the large-scale structure which surrounds them.

So far, we have only discussed the model at a fixed redshift. Since the barrier shapes depend on redshift, our approach also allows one to estimate how sheet, filament and halo abundances evolve. Moreover, it allows one to address questions like: is the halo abundance in sheets of mass $10^{15} M_\odot$ at $z = 1$ any different from the mix of halos in $10^{15} M_\odot$ filaments today?

Our model naturally incorporates the fact that the mass in high redshift sheets becomes partitioned up among filaments at later times, with filaments themselves being partitioned into halos. Clearly, the model is rich in spatial, temporal and spatio-temporal information.

2.3. Mass dependence of the three barriers

The key output from the triaxial collapse models is an estimate of the typical overdensity required for collapse along one, two and three axes by redshift z . The dotted curves in Figure 1 show how these three ‘barriers’ depend on mass. From bottom to top, the curves show

$$\begin{aligned}\delta_{ec1}(\sigma, z) &= \delta_{sc}(z) \left\{ 1 - 0.56 \left[\frac{\sigma^2}{\delta_{sc}^2(z)} \right]^{0.55} \right\}, \\ \delta_{ec2}(\sigma, z) &= \delta_{sc}(z) \left\{ 1 - 0.012 \left[\frac{\sigma^2}{\delta_{sc}^2(z)} \right]^{0.28} \right\} \approx \delta_{sc}(z), \\ \delta_{ec3}(\sigma, z) &= \delta_{sc}(z) \left\{ 1 + 0.45 \left[\frac{\sigma^2}{\delta_{sc}^2(z)} \right]^{0.61} \right\}.\end{aligned}\quad (2)$$

These analytic approximations to the barriers associated with collapse along one, two and three axes are reasonably accurate (c.f. Figure 7). They show that the critical overdensity for ellipsoidal collapse along all three axes, δ_{ec3} , is larger than in the spherical collapse model (for which this number is δ_{sc}). However, collapse along just two axes requires an overdensity δ_{ec2} which is almost exactly that in the spherical model, and collapse along one axis only requires a smaller initial overdensity, δ_{ec1} . In this model, tidal forces enhance collapse along the first axis and delay collapse along the last axis relative to the spherical collapse model (Sheth et al. 2001)—the expressions above quantify these effects. Note that the differences among the three critical overdensities are larger for larger values of σ , corresponding to ellipsoids of lower masses.

Notice that these barrier shapes depend both on $\sigma(m)$ and on $\delta_{sc}(z)$. The presence of these two terms reflects the fact that the collapse depends on the expansion history of the universe, and on the initial spectrum of fluctuations. What is of particular importance in what follows is that the barrier shapes actually depend, not on δ_{sc} and σ individually, but on the scaling variable $\nu = [\delta_{sc}(z)/\sigma(m)]^2$. In the excursion set approach, this implies that the mass functions of sheets, filaments and halos at any given time, in any given cosmology, and for any given initial fluctuation spectrum, can all be scaled to universal functional forms. Our next step is to provide analytic approximations to these forms.

2.4. First crossing distributions

In the simplest excursion set model, object abundances are related to the first crossing distributions by one-dimensional random walks of the moving barriers in equation (2). These distributions are easily obtained by Monte-Carlo simulation. (Alternative numerical methods are also available, e.g., Zhang & Hui 2006.) The Monte-Carlo results are simplified considerably by the fact that the barriers can be expressed in terms of the scaling variable $\nu = [\delta_{sc}(z)/\sigma(m)]^2$. The histograms in Figure 2 show the results. The abundances of sheets, filaments and halos are related to these first crossing distributions by equation (1).

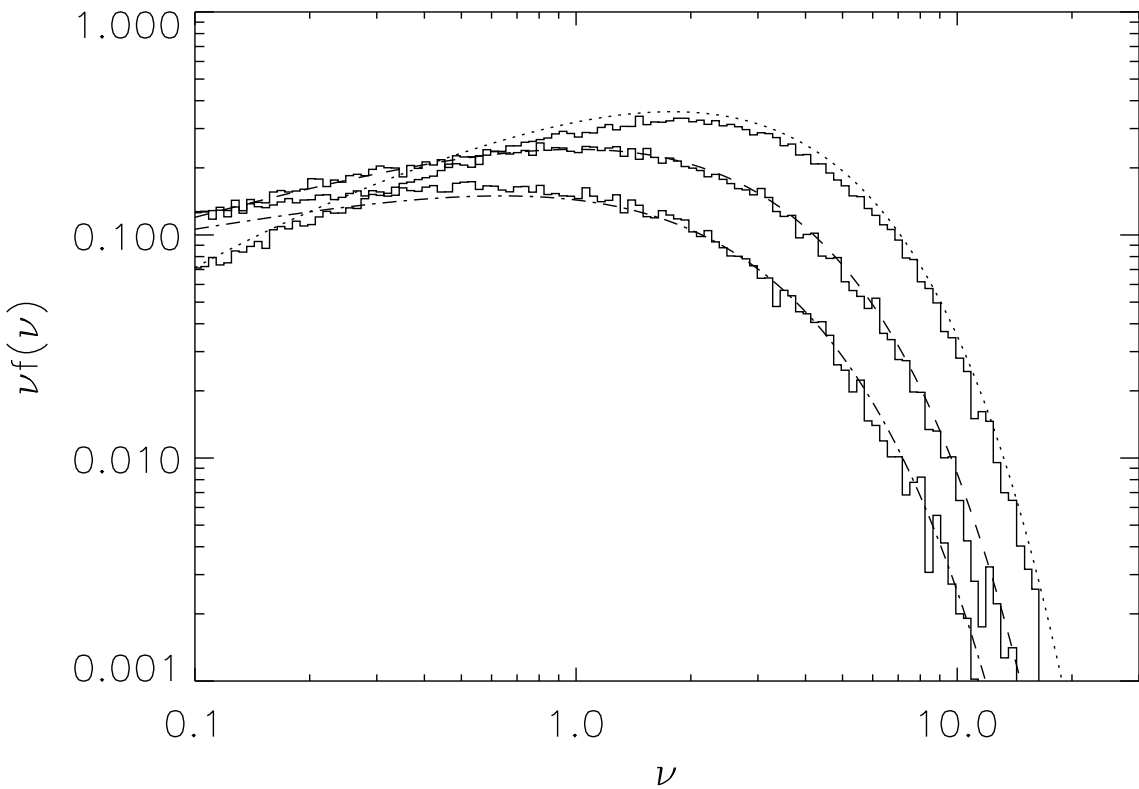


Fig. 2.— Histograms show the first crossing distributions of the barriers associated with collapse along one, two and three axes (histograms which extend to largest ν are those for collapse along only one axis). Curves show analytic approximations to these distributions following Sheth & Tormen (2002).

The smooth curves show analytic approximations to these first crossing distributions, com-

puted following Sheth & Tormen (2002). Namely, when the barrier is of the form

$$\delta_{ec}(\sigma, z) = \delta_{sc}(z) \left[1 + \beta \nu^{-\alpha} \right], \quad (3)$$

as is the case for all three barriers in equation (2), then the first crossing distribution is approximately

$$\nu f(\nu) = \sqrt{\frac{\nu}{2\pi}} e^{-\nu[1+\beta\nu^{-\alpha}]^2/2} \left\{ 1 + \frac{\beta}{\nu^\alpha} \left[1 - \alpha + \frac{\alpha(\alpha-1)}{2!} + \dots \right] \right\}. \quad (4)$$

Alternative analytic estimates could be computed by noting that when $\alpha = 1/2$, then the first crossing distribution can be written analytically in terms of sums of parabolic cylinder functions (Breiman 1967). Given that these would only provide approximations to the first crossing distributions we require (because $\alpha \neq 1/2$), we have chosen the considerably simpler approximation given in equation (4). Figure 2 indicates that these approximate solutions are sufficiently accurate to allow analytic estimates of a number of interesting quantities.

2.5. Abundance by mass and redshift

Upon assumption of a cosmology [which determines $\delta_{sc}(z)$] and a fluctuation spectrum [which determines $\sigma(m)$], the first crossing distributions shown in Figure 2 can be converted to mass functions using equation (1). In what follows, we assume a spatially flat model with cosmological constant $\Lambda_0 = 1 - \Omega_0$, where $(\Omega_0, h, \sigma_8) = (0.3, 0.7, 0.9)$.

The dashed lines in the bottom-left panel of Figure 3 show the evolution of the number densities of halos having mass $10^{10} M_\odot$ (top) to $10^{15} M_\odot$ (bottom). Except for the lowest mass range, these curves decrease monotonically with increasing redshift. This reflects the well-known hierarchical nature of structure formation: at any given redshift, massive halos are less common than halos of lower mass, and they are even less common at earlier times. As a result, if one integrates the mass fraction in objects above some minimum mass, then this fraction is smaller at higher redshift. If, instead, one fixes the mass fraction, then one must integrate down to smaller mass halos to obtain this fraction. Since less massive halos are more abundant, plots of the abundance associated with a fixed mass fraction increase with increasing redshift (Mo & White 2002). The solid curves show such locii in the abundance-redshift plane for a range of mass fractions. The top-left and right panels show analogous results, but for sheets and filaments respectively. Similar trends are seen in all three panels, indicating that sheets and filaments grow hierarchically in much the same way as halos.

These panels show that, at $z = 0$, more than half of the cosmic mass is in sheets with masses exceeding $10^{13} M_\odot$. This fraction is about 30% for filaments in the same mass range, and is

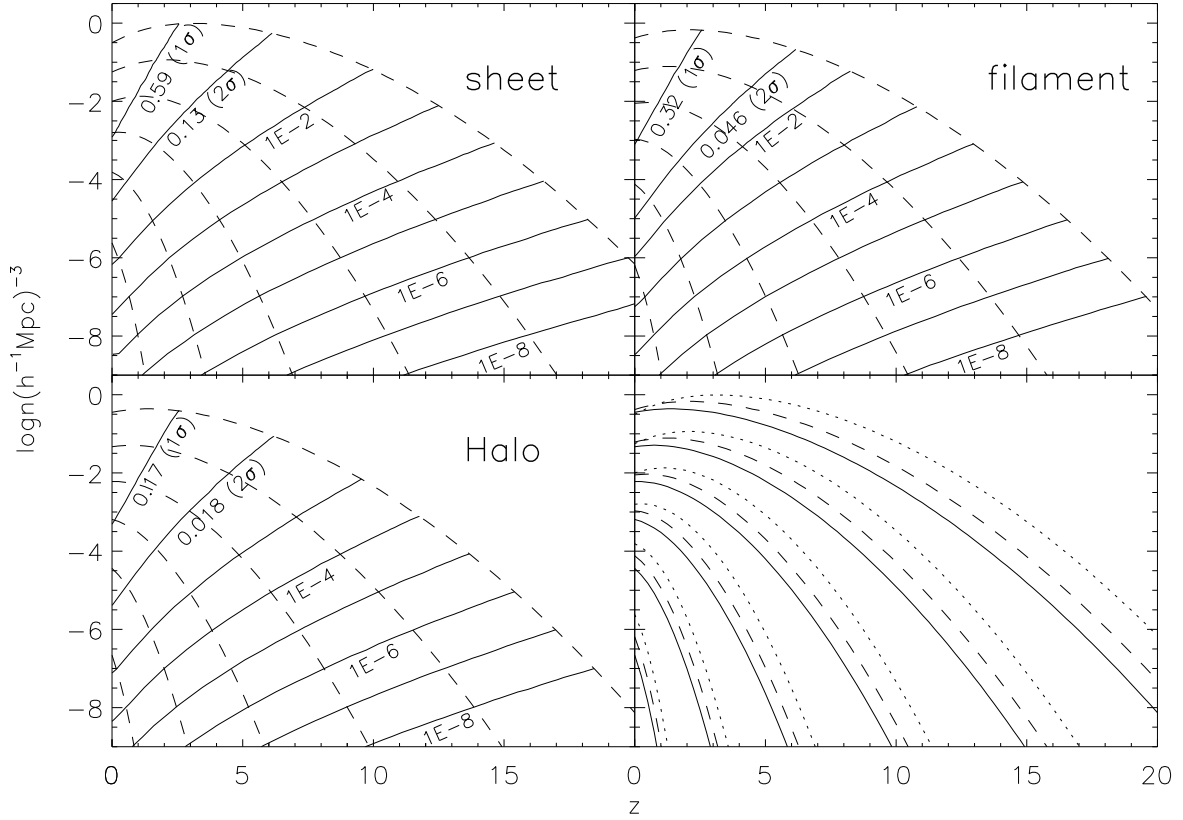


Fig. 3.— The upper left, upper right and bottom left are the comoving number densities (dashed lines) and mass fractions (solid lines) for sheets filaments and halos respectively. The bottom right of the figure compares the comoving number densities of sheets (dotted lines), filaments (dashed lines) and halos (solid lines). The top sets of curves are for objects with masses of $10^{10} M_{\odot}$, and subsequent curves show masses which are larger by 1 dex until the bottom sets of curves, which are for masses of $10^{15} M_{\odot}$.

only 13% for halos. At the present time, more than 99% of the cosmic mass is contained in sheets more massive than $10^{10} M_{\odot}$, in contrast to virialized halos which, in this mass range, contain only about half of the cosmic mass. At $z \sim 3$, more than 10% of the cosmic mass was already assembled in sheets more massive than that of the Milky Way halo ($\sim 10^{12} M_{\odot}$), while only 2% was assembled to halos in this mass range. Even at $z \sim 10$, more than 1% of the cosmic mass was already in sheets more massive than $10^{10} M_{\odot}$, whereas the mass fraction in halos in the same mass range was ten times smaller. This suggests that the structure at high z is dominated by sheets.

At any given redshift, we may define a characteristic mass, $M_*(z)$, so that $\sigma(M_*)$ is equal to the critical overdensity $\delta_{sc}(z)$. In our Λ CDM model, the value of M_* drops rapidly with redshift, from just over $10^{13} M_\odot$ at $z = 0$ to $\sim 10^{10.5} M_\odot$ at $z = 2$. Objects at z whose mass satisfies $\sigma(M) = N\delta_{sc}(z) = N\sigma(M_*)$, where $N = 1, 2, \dots$, can be thought of as being increasingly unusual compared to objects of the characteristic mass $M_*(z)$. The top two solid curves in the first three panels of Figure 3 show the abundance-redshift locii of sheets, filaments and halos whose masses satisfy $\sigma(M) = \sigma(M_*)$ and $\sigma(M) = 2\sigma(M_*)$. The panels show that the mass fraction in 1σ sheets, 0.59, is larger than that in 1σ filaments (0.32) and than that in 1σ halos (0.17). A similar scaling applies to the more massive 2σ objects, implying that, at any redshift, the typical structure is dominated by sheets.

The bottom right panel in Figure 3 compares the number densities of sheets (dotted), filaments (dashed) and halos (solid) at different redshifts in the three other panels directly (i.e., these were the dashed curves in the other three panels): top-most curves show our model for masses of $10^{10} M_\odot$, bottom-most for $10^{15} M_\odot$, and the curves in between show results in which the mass changes by 1 dex. These curves show that, at masses larger than $10^{12} M_\odot$, there are more sheets than filaments, and more filaments than halos, for almost all redshifts. However, at small masses and late times this trend begins to reverse: at $z = 0$ there are fewer sheets than filaments with masses smaller than $10^{11} M_\odot$, and there are more halos than sheets of mass $10^{10} M_\odot$. Based on these mass functions, we can estimate the average mass of objects more massive than some given minimum mass. For instance, when the minimum mass is $10^{10} M_\odot$ then, at the present time, this average mass is $3.9 \times 10^{11} M_\odot$ for sheets, $2.1 \times 10^{11} M_\odot$ for filaments, and $1.6 \times 10^{11} M_\odot$ for halos. The average mass of sheets is about 2.5 times that of halos, again suggesting that large scale structure is dominated by sheets rather than by virialized halos.

2.6. Conditional mass functions

Halo abundances are expected to correlate with the overdensity of their surroundings—massive halos populate dense regions (Mo & White 1996). However, our model predicts that halo abundances will also correlate with the morphology of their surroundings. To illustrate, the solid curve in Figure 4 shows the mass fraction of $10^{13} M_\odot$ sheets that is in filaments of mass m at $z = 0$. The figure indicates that the most probable filament mass, $7 \times 10^{12} M_\odot$, is a substantial fraction of that of its parent sheet. Although we do not show it, the analytic estimate of this quantity, given by inserting our barriers for filaments and sheets in equation (7) of Sheth & Tormen (2002), is in excellent agreement with this distribution. This solid curve should be compared with the dashed one, which shows the mass fraction in halos (rather than filaments) of mass m that are known to be in sheets of mass $10^{13} M_\odot$.

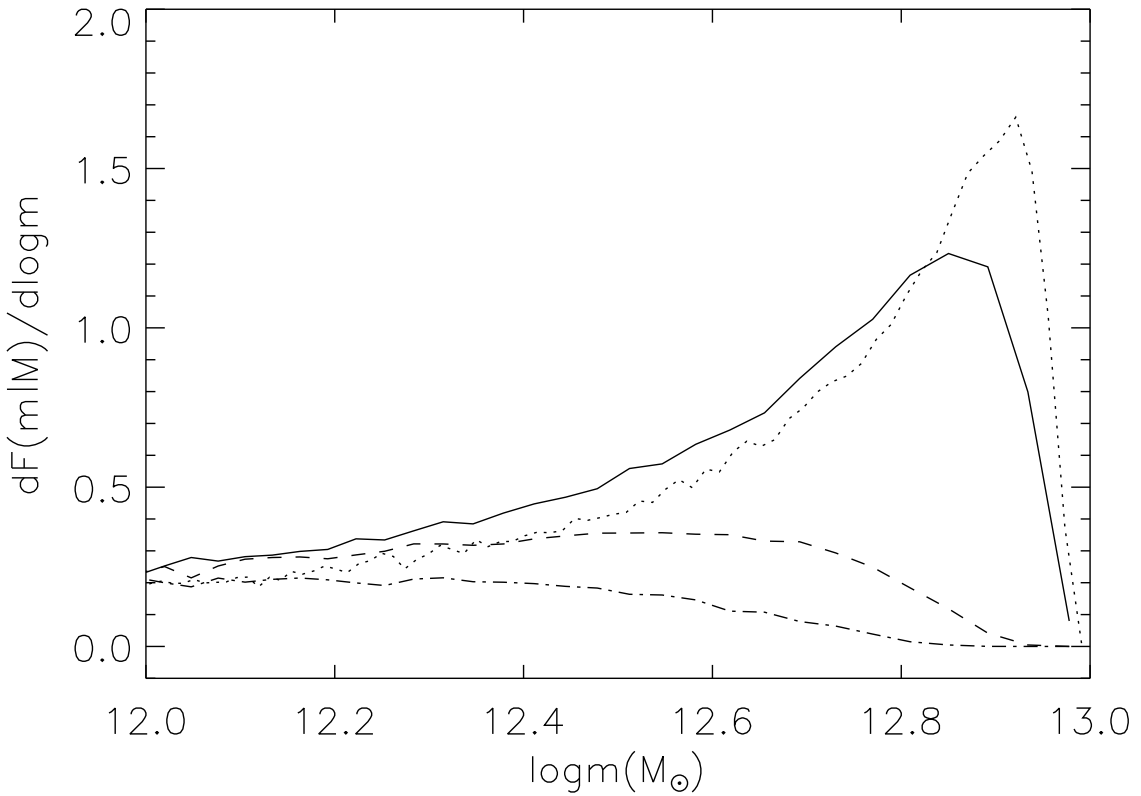


Fig. 4.— Mass fraction of $10^{13} M_{\odot}$ sheets that is in filaments (solid) and halos (dashed) of mass m all at $z = 0$. Dotted curve shows the mass fraction of $10^{13} M_{\odot}$ filaments at $z = 0$ that is in halos. Dot-dashed curve shows the mass fraction contained in halos of mass m within an average volume of the universe of the same mass ($10^{13} M_{\odot}$). The differences between the dotted and dashed curves indicate that, at fixed large-scale overdensity, the halo population is expected to be correlated with the morphology of the surrounding large-scale structure.

at $z = 0$. (In this case, the analytic estimate is not as accurate.) Notice that the most probable halo mass is significantly smaller than that of the parent sheet, and the halo mass function in sheets is skewed significantly towards lower masses than that of filaments. As a final comparison, the dotted line shows the mass fraction of $10^{13} M_{\odot}$ filaments (rather than sheets) that is in halos of mass m , and the dot-dashed curve shows the mass fraction contained in halos of mass m within an average volume of the universe of the same mass ($10^{13} M_{\odot}$). Here again, the mass function within sheets and filaments is biased compared to the average universe and the most probable halo mass is a substantial fraction of the mass

of the parent filament. The significant differences between the dotted and dashed curves illustrate an important physical implication of our model: if the properties of a galaxy are correlated with the mass of its host halo, then the galaxy population in sheets of a given mass is expected to be different from that in filaments of the same mass. In other words, at fixed large-scale mass, galaxy properties are expected to be correlated with the morphology of the surrounding large scale structure.

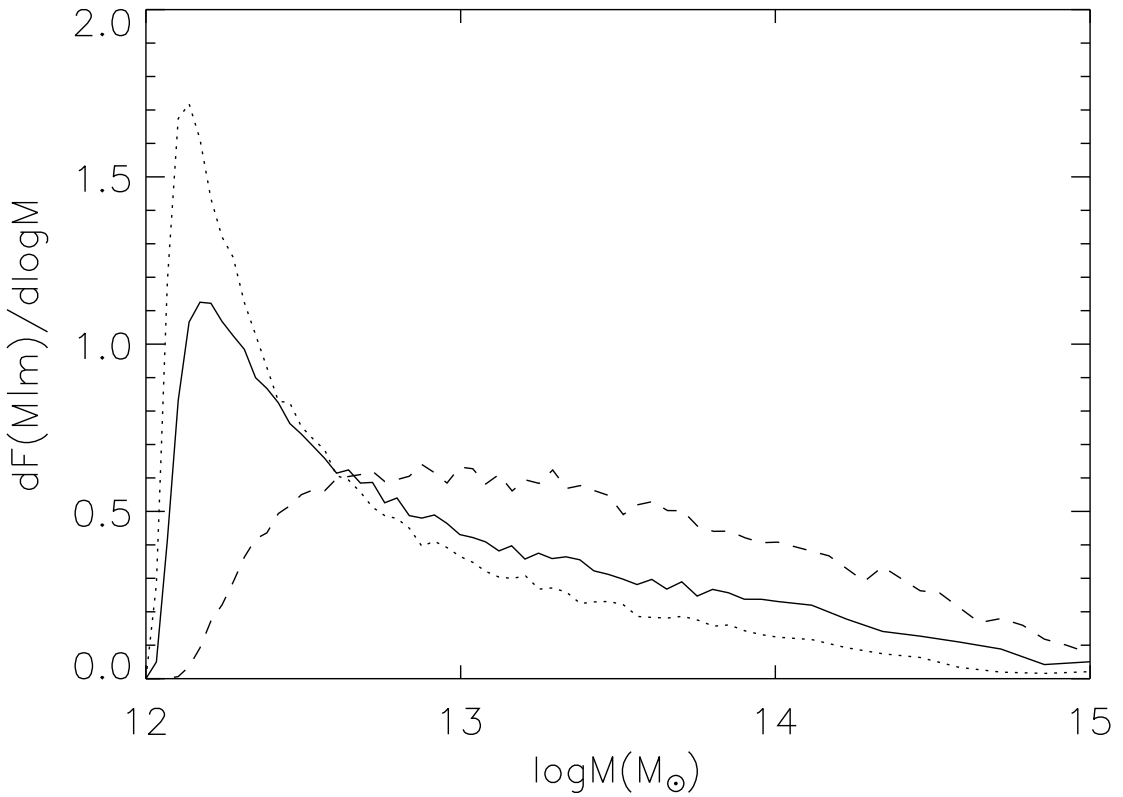


Fig. 5.— Conditional distribution of sheets centred on a smaller scale filament of mass $10^{12} M_\odot$ (solid). Dotted and dashed curves show the distribution of filaments and sheets which surround $10^{12} M_\odot$ halos.

Figure 4 shows the distribution of masses of smaller scale objects when the large scale mass and morphology is fixed. But our model also allows one to estimate the mass and morphology of the environment which surrounds a given smaller scale structure. To illustrate, Figure 5 shows conditional mass functions in which the small-scale object is fixed, and we study the distribution of the surrounding large scale mass and morphology. The solid curve shows

the distribution of sheets around $10^{12} M_\odot$ filaments, and the dotted and dashed curves show the distributions of filaments and sheets around $10^{12} M_\odot$ halos. (Once again, the analytic estimates of these distributions are in reasonable but not perfect agreement.) Notice again that the mass of a sheet is well correlated with the mass of the filament it surrounds, as are the masses of filaments with those of the halos they surround. On the other hand, halo and sheet masses can be very different. These scalings indicate that our model can be used to estimate how the surrounding large scale structure correlates with different galaxy populations.

2.7. Filamentary versus isotropic mass growth

Our model can be used to provide a simple estimate of how halos grow. To see why, consider a random walk with height equal to the rms fluctuation: σ . The typical mass scales of sheets, filaments and halos are given by setting this value equal to the various barrier heights: $\sigma = \delta_{\text{ec}1,2,3}(\sigma, z)$. To see what this implies, approximate the three moving barriers in equation (2) as

$$\begin{aligned}\delta_{\text{ec}1}(\sigma, z) &\approx \delta_c(z) \left\{ 1 - 0.5 \frac{\sigma}{\delta_c(z)} \right\} = \delta_c(z) - 0.5 \sigma; \\ \delta_{\text{ec}2}(\sigma, z) &\approx \delta_c(z); \\ \delta_{\text{ec}3}(\sigma, z) &\approx \delta_c(z) \left\{ 1 + 0.5 \frac{\sigma}{\delta_c(z)} \right\} = \delta_c(z) + 0.5 \sigma.\end{aligned}$$

Then the typical mass scale of filaments is $\sigma_f \approx \delta_c(z)$. Similarly, a characteristic mass scale for sheets is $\sigma_s \approx \delta_c(z) - 0.5 \sigma_s$, implying $\sigma_s = (2/3) \sigma_f$, whereas the mass scale of halos is $\sigma_h = 2 \sigma_f$.

Massive objects are associated with more extreme fluctuations. We can approximate by studying the case in which the walk height is twice the rms value (a 2σ fluctuation). In this case, $\sigma_f = \delta_c(z)/2$, $\sigma_s = (2/5) \delta_c(z) = (4/5) \sigma_f$, and $\sigma_h = (2/3) \delta_c(z) = (4/3) \sigma_f$. Notice that, for massive objects, these factors are substantially closer to unity than they are for more typical objects. This suggests that the most massive halos are a substantial fraction of the mass of the filaments they populate, and these filaments are a substantial fraction of the sheets in which they are embedded. Thus, massive halos will appear to be accreting most of their mass from filaments. In contrast, a lower mass halo may be substantially less massive than the filament it inhabits. The growth of such a halo will appear to be dominated by mergers with the other small halos which populate the same filament (and possibly the other nearby filaments). In this respect, our model is qualitatively consistent with observations which suggest that massive clusters grow by accretion along filaments, whereas the growth of lower mass objects is less obviously anisotropic.

2.8. Identification of sheets, filaments and halos in the cosmic web

Although our approach provides a framework for discussing the morphology of the cosmic web, we have, so far, not made any statements about precisely how the sheets, filaments and halos in our formalism are to be identified in cosmic density fields. Our collapse model is calibrated so that the object which forms after collapse has been completed along all three axes, i.e., a halo, has the same density relative to the background as is expected in the spherical collapse model. Sheets in our model should be approximately this overdensity to the one-thirds power, whereas filaments are this to the two thirds power. Although, formally, the density of a halo depends on the background cosmological model, it is common practice to identify halos at a given epoch as objects which are 200 times denser than the critical density at that epoch. Therefore, filaments and sheets should be approximately 36 and 6 times denser than the critical density. This provides a simple rule of thumb for identifying sheets and filaments in the dark matter density field. Note that, in the context of our model, it may be more appropriate to think of massive halos as lying at the centers of filaments, rather than defining their endpoints. It will be interesting to see how these simple estimates compare with measurements in simulations.

3. Discussion and Conclusion

We extend the excursion set approach to quantify how the cosmic web is made up of sheets, filaments and halos. Our model assumes that objects form from a triaxial collapse; we define sheets as objects which have collapsed along only one axis, filaments as objects which have collapsed along two axes, and halos as objects where all three axes have collapsed. Therefore, our model requires specification of exactly how triaxial collapse occurs. Appendix A discusses our preferred collapse model, compares it with Zeldovich's approximation, and shows how the analytic arguments of White & Silk (1979) can be extended to provide an accurate analytic description of our ellipsoidal collapse model.

The details of how a patch collapses depends on its initial overdensity δ , and on its initial shape parameters e and p . To embed this collapse model in the excursion set approach requires study of three-dimensional random walks crossing a barrier $B(\delta, e, p)$. Here, we follow Sheth et al. (2001) and study the simpler problem in which e and p are replaced by representative values, and then study a one-dimensional boundary crossing problem. We emphasize that this is only an approximation, albeit a useful one.

For any redshift z , insertion of the representative values of e and p in our collapse model provides estimates of the critical overdensities required for collapse along one, two and three axes. We find that these overdensities, $\delta_{ec1}(z, \sigma)$, $\delta_{ec2}(z, \sigma)$ and $\delta_{ec3}(z, \sigma)$ depend on both time

and mass (equation 2). Because of the dependence on σ , in the language of the excursion set approach, each of these critical overdensities is a ‘moving barrier’ (Figure 1). Insertion of each moving barrier into the excursion set approach provides estimates of the mass fraction in sheets, filaments and halos as a function of mass and time (Figure 2).

In our model, halos of a given mass m_h populate filaments which are more massive, and the filaments themselves are surrounded by even more massive sheets. Hence, the characteristic masses of sheets are predicted to be substantially larger than of filaments or halos. Every halo at a given time was previously a filament of the same mass, and before that, a sheet. A halo of mass $10^{13} M_\odot$ today was a filament at redshift $z \approx 0.45$ and a sheet at $z \approx 1$ (c.f. equation 2). Halo abundances are expected to correlate with the overdensity of their surroundings (massive halos populate dense regions). Our model predicts that, at fixed large-scale overdensity, halo abundances will also correlate with the morphology of their surroundings (Figures 4 and 5). Therefore, in models where the properties of a galaxy are correlated with the mass and formation history of its host halo, our model provides a framework for describing correlations between galaxy properties and the morphology of large scale structure. For instance, distributions like those in Figure 4 may be used to study if morphological structures in the galaxy distribution, like the SDSS Great Wall at $z \sim 0.08$, are unusual. And distributions like those in Figure 5 provide a framework for understanding if galaxies at high redshift form preferentially in sheets or filaments (Mo et al. 2005). Because our model exhibits various physically appealing features, we anticipate that it will provide a useful framework for quantifying the relation between galaxies, halos, and the cosmic web.

We would like to thank Gerhard Börner for organizing a meeting at the Ringberg Castle, Tegernsee, and the staff of the Castle for their hospitality when this project began. We thank Joerg Colberg and an anonymous referee for insightful comments and questions. JS thanks the University of Massachusetts at Amherst for hospitality during the summer of 2004. This work was supported by the NSF under CAREER award AST-0239709 to TA, and grant AST-0520647 to RKS.

REFERENCES

Bharadwaj, S., Sahni, V., Sathyaprakash, B.S., Shandarin, S.F., Yess, C., 2000, ApJ, 528, 21

Bharadwaj, S., & Biswajit, P., 2004, ApJ, 615, 1

Bhavsar, S.P. Ling, E.N., 1988, ApJ, 331, L63

Bhavsar, S., Bharadwaj, S., Sheth, J., 2003, AIP Conference Proceedings, 666, 303

Biswajit, P., & Bharadwaj, S., 2005, MNRAS, 357, 1068

Breiman, L., 1967, 5th Berkeley Symp. 2(2): 9

Bond, J.R., Cole, S., Efstathiou, G., Kaiser, N., 1991, ApJ, 379, 440

Bond, J.R., & Myers, S., 1996, ApJS, 103, 1

Bond J. R., Kofman L., Pogosyan D., 1996, Nature, 380, 603

Chiueh, T., & Lee, J., 2001, ApJ, 555, 83

Colberg J., Krughoff S., Connolly A., 2005, MNRAS, 359, 272

Doroshkevich, A.G., 1970, Astrofizika, 3, 175

Efstathiou, G., Frenk, C. S., White, S.D.M., Davis, M., 1988, MNRAS, 235, 715

Eisenstein, D.J., Loeb A., 1995, ApJ, 439, 520

Gregory, S.A., Thompson L. A., 1982, Scientific American, 246, 106

Gunn J.E., Gott J.R. III, 1972, ApJ, 176, 1

Gurbatov S. N., Saichev A. I., Shandarin S. F., 1989, MNRAS, 236, 385

Icke, V., 1973, A&A, 27, 1

Jing, Y.P., Suto, Y., 2002, ApJ, 574, 538

Kirshner R. P., Oemler A., Schechter P. L., Schechter S. A., 1983, IAUS, 104, 197

Lee, J., Shandarin, S.F., 1998, ApJ, 500, 14

Mo H.J., White S.D.M., 1996, MNRAS, 282, 347

Mo H.J., White S.D.M., 2002, MNRAS, 336, 112

Mo H.J., Yang X., van den Bosch F.C., Katz N., 2005, MNRAS, 363, 1155

Monaco, P., 1995, ApJ, 447, 23

Müller V., Arbabi S., Maulbetsch C., 2003, IAUS, 216, 79

Peebles P.J.E., 1980, The Large-Scale Structure of the Universe, Princeton University Press

Press, W., Schechter, P., 1974, ApJ, 187, 425

Shandarin, S.F., Sheth, J.V., & Sahni, V. 2004, MNRAS, 353, 162

Sheth, J.V., Sahni, S., Shandarin, S.F., & Sathyaprakash, B.S. MNRAS, 2003, 343, 22

Sheth R. K., Tormen G., 1999, MNRAS, 308, 119

Sheth, R.K., Mo, H.J., Tormen, G., 2001, MNRAS, 323, 1

Sheth, R.K., Tormen, G., 2002, MNRAS, 329, 61

Sheth, R.K., van de Weygaert, R, 2004, MNRAS, 350, 517

Vogeley M. S., Hoyle F., Rojas R. R., Goldberg D. M., 2004, IAUC, 195, 5

White, S.D.M., Silk, J., 1979, ApJ., 231, 1

Zeldovich, Ya.B., 1970, A&A, 5, 84

A. Appendix

This Appendix describes the triaxial collapse model we use in the main text. Although the evolution must be solved numerically in general, we also discuss a reasonably accurate analytic approximation to the evolution, and show that it is considerably more accurate than the Zeldovich approximation.

Let A_k denote the scale factors for the three principal axes of the ellipsoid. Then

$$\frac{d^2 A_k}{dt^2} = -4\pi G \bar{\rho} A_k \left[\frac{1+\delta}{3} + \frac{b'_k}{2} \delta + \lambda'_{\text{ext}k} \right] \quad (\text{A1})$$

(Bond & Myers 1996), where $\bar{\rho} \propto a^{-3}$ is the mean density of the universe,

$$\delta \equiv \frac{\rho - \bar{\rho}}{\bar{\rho}} = \frac{a^3}{A_1 A_2 A_3} - 1 \quad (\text{A2})$$

is the relative overdensity, and $b'_k \delta / 2$ and $\lambda'_{\text{ext}k}$ denote the interior and exterior tidal forces. In particular,

$$b'_k(t) = b_k(t) - \frac{2}{3}, \quad \text{where } b_k(t) = A_1(t) A_2(t) A_3(t) \int_0^\infty \frac{d\tau}{[A_k^2(t) + \tau] \prod_{m=1}^3 [A_m^2(t) + \tau]^{1/2}}, \quad (\text{A3})$$

and the linear approximation for the external tides is

$$\lambda'_{\text{ext}k}(t) = \frac{a}{a_i} \lambda'_k(t_i) = \frac{a}{a_i} \left[\lambda_k(t_i) - \frac{\delta_i}{3} \right], \quad (\text{A4})$$

where $a_i = a(t_i)$. Note that the λ_k s are the initial eigenvalues of the strain tensor; they are related to the initial density contrast δ_i and the shear ellipticity e and prolateness p by:

$$\lambda_1 = (\delta_i/3)(1 + 3e + p), \quad \lambda_2 = (\delta_i/3)(1 - 2p), \quad \text{and} \quad \lambda_3 = (\delta_i/3)(1 - 3e + p). \quad (\text{A5})$$

The initial conditions are set by Zeldovich approximation:

$$A_k(t_i) = a_i[1 - \lambda_k(t_i)], \quad \text{and} \quad \dot{A}_k(t_i) = H(t_i)A_k(t_i) - a_iH(t_i)\lambda_k(t_i). \quad (\text{A6})$$

These expressions reduce to those of the spherical collapse model if the two tidal force terms are not included. Note that, as a result of the tidal forces, an initially spherical region will be distorted into a collapsing homogeneous ellipsoid.

The tidal gravitational forces accentuate the asymmetry of the ellipsoid, so that the collapse of the three axes can happen at very different times. The shortest axis will collapse first, followed by the intermediate axis and then by the longest axis. Absent angular momentum, the collapse of any given axis continues to arbitrarily small sizes, a well-known feature of the spherical collapse model as well.

Given initial values of δ_i , ellipticity e , prolateness p , and epoch a_i , equation (A1) must be solved numerically for each axis A_k . However, it is straightforward to extend the analytic approximation for ellipsoidal collapse provided by White & Silk (1979) so that it reduces self-consistently to the Zeldovich approximation at early times. In particular, we write

$$A_k(t) \approx \frac{a(t)}{a_i} A_k(t_i) \left[1 - D(t) \lambda_k \right] - \frac{a(t)}{a_i} A_h(t_i) \left[1 - \frac{D(t)\delta_i}{3} - \frac{a_e(t)}{a(t)} \right], \quad (\text{A7})$$

where $A_h(t_i) = 3 / \sum_k A_k(t_i)^{-1}$, $D(t)$ is the linear theory growth mode, and $a_e(t)$ is the expansion factor of a universe with initial density contrast $\delta_i \equiv \sum_k \lambda_k(t_i)$. Note that the first term in the expression above is the Zeldovich approximation to the evolution. Also note that, if all three axis are initially the same, then all the λ_j s are the same, and $\lambda = \delta_i/3$. In this case, the perturbation is a sphere, and the expression above reduces to $A(t) \rightarrow A(t_i) [a_e(t)/a_i]$, so the approximation (A7) is exact.

Figure 6 compares the full numerical evolution of the three axes in this model (solid) with the Zeldovich approximation (dotted) and with equation (A7) (dashed), when the initial values are $(\delta, e, p) = (2/400, 0.2, 0)$ in an Einstein de-Sitter universe. This shows clearly that, at late times, equation (A7) is significantly more accurate than the Zeldovich approximation.

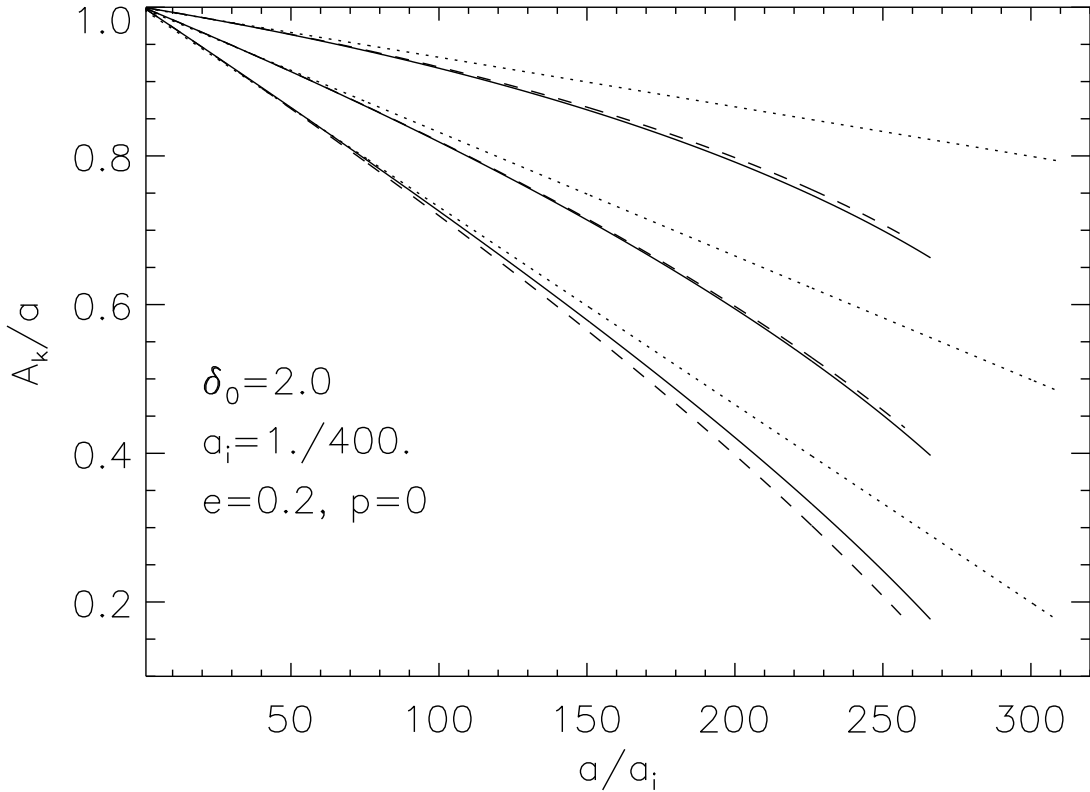


Fig. 6.— Comparison of full ellipsoidal collapse model (solid), Zeldovich approximation (dotted) and the approximation in equation (A7) for $e = 0.2$ and $p = 0$ in an Einstein de-Sitter model. The three sets of curves show the comoving lengths of the shortest, intermediate and longest axes. These correspond to the formation of sheets, filaments and halos.

The numerical solution allows each axis to shrink to arbitrarily small sizes. In studies of the spherical evolution model it is standard to assume that virial equilibrium leads to a non-negligible freeze-out radius. For an Einstein de-Sitter model, this freeze-out radius is $A_k = 0.177a$, so the final object is $18\pi^2 \approx 178$ times denser than the background universe. Bond & Myers (1996) suggested that this same factor could be used in the ellipsoidal collapse model as well: hence, we stop the collapse of axis k by hand when $A_k/a = 0.17$.

Thus, in this model, initial values of λ_k and a_i yield initial values of δ_i , e and p . The collapse model then provides an estimate of the times at which each axis freezes-out. In particular, note that if e and p are given, then there is a unique value of δ_i which will produce collapse of the k th axis at redshift z . The symbols in Figure 7 show the critical densities for collapse

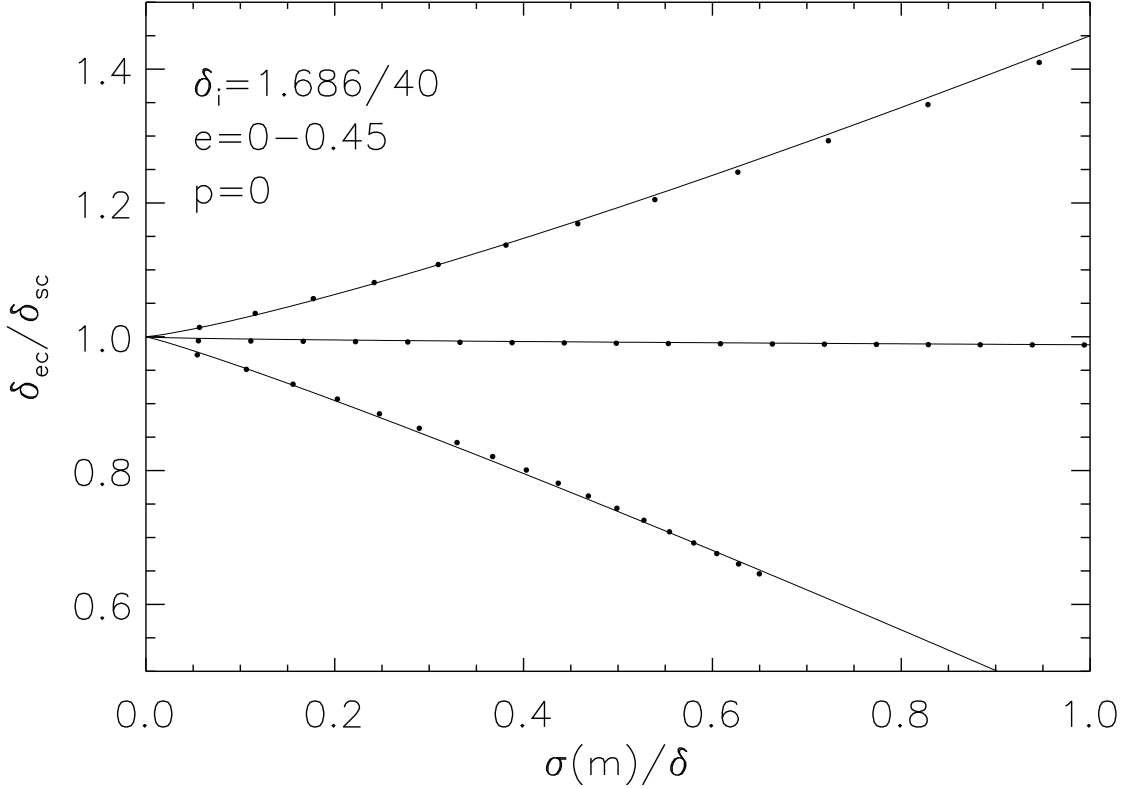


Fig. 7.— Dependence of barrier height on mass for collapse along one, two and three axes (bottom to top). Symbols show the relations determined from the ellipsoidal collapse model, and curves show the analytic forms given in the main text (equation 2).

at $z = 0$ when $p = 0$ and $e = (\sigma/\delta)/\sqrt{5}$ along one (bottom), two (middle) and three (top) axes. In the random walk model discussed in the main text, these values of e and p , and this relation between the critical density required for collapse at z and the initial shape play a central role. The solid curves show the simple fits to these relations given in equation (2).

Notice that the critical density for collapse of the second axis is *very* similar to that for a spherical model. The approximation (A7) provides an easy way to see why. First, note that to second order in δ_i ,

$$\frac{A_h(t_i)}{a_i} \approx 1 - \frac{\delta_i}{3} - 2(3e^2 + p^2) \left(\frac{\delta_i}{3}\right)^2. \quad (\text{A8})$$

Second, recall that when $p = 0$ then $\lambda_2 = \delta_i/3$. Third, when $p = 0$ and $e = (\sigma/\delta)/\sqrt{5}$ (our representative values) then the final term in the expression above is $(2/15)\sigma_i^2$, so $A_h(t_i) \approx$

$A_2(t_i) - a_i (2/15)\sigma_i^2$. Therefore, for $\sigma_i \ll 1$,

$$\frac{A_2(t)}{A_2(t_i)} \approx \frac{a(t)}{a_i} \left[1 - D(t) \lambda_2 \right] - \frac{a(t)A_h(t_i)}{a_i A_2(t_i)} \left[1 - \frac{D(t)\delta_i}{3} - \frac{a_e(t)}{a(t)} \right] \approx \frac{a_e(t)}{a_i}; \quad (\text{A9})$$

in this approximation, the second axis evolves *exactly* as in a spherical model with initial overdensity δ_i .